Received: 12 May 2017 | Revised: 24 August 2017 | Accepted: 7 November 2017

DOI: 10.1111/ter.12315

PAPER

WILEY Terra Nova

What can strike-slip fault spacing tell us about the plate boundary of western North America?

Andrew V. Zuza | Chad W. Carlson

Nevada Bureau of Mines and Geology, University of Nevada, Reno, NV, USA

Correspondence
Andrew V. Zuza, Nevada Bureau of Mines and Geology, University of Nevada, Reno, NV, USA.
Email: azuza@unr.edu; avz5818@gmail.com

Funding information
University of Nevada, Reno

Abstract

The spacing of parallel continental strike-slip faults can constrain the mechanical properties of the faults and fault-bounded crust. In the western US, evenly spaced strike-slip fault domains are observed in the San Andreas (SA) and Walker Lane (WL) fault systems. Comparison of fault spacing (*S*) vs. seismogenic zone thickness (*L*) relationships of the SA and WL systems indicates that the SA has a higher *S*/*L* ratio (~8 vs. 1, respectively). If a stress-shadow mechanism guides parallel fault formation, the *S*/*L* ratio should be controlled by fault strength, crustal strength, and/or regional stress. This suggests that the SA-related strike-slip faults are relatively weaker, with lower fault friction: 0.13–0.19 for the SA vs. 0.20 for WL. The observed mechanical differences between the San Andreas and Walker Lane fault systems may be attributed to variations in the local geology of the fault-hosting crust and/or the regional boundary conditions (e.g. geothermal gradient or strain rate).

1 | INTRODUCTION

Parallel strike-slip faults are observed at a variety of scales, from continental faults that cut through the entire brittle crust to millimeter-scale faults in outcrops and analogue experiments (Davy & Cobbold, 1988; Dickinson, 1996; Martel & Pollard, 1989; Segall & Pollard, 1983). Analyses of active strike-slip faults in central Asia and California suggest that a modified stress-shadow mechanism (Lachenbruch, 1961) controls fault spacing (Yin, Zuza, & Pappalardo, 2016; Zuza, Yin, Lin, & Sun, 2017). Accordingly, the characteristic fault spacing (*S*) is linearly related to the brittle-layer thickness (*h*) (i.e. the seismogenic zone) of a deforming layer as a function of fault strength, crustal strength, and regional stress.

We examined parallel strike-slip fault domains along the western plate boundary of North America to understand the development of the San Andreas (SA) and Walker Lane (WL) fault systems (Figure 1) in the context of continental-scale stress shadows. These faults are ideal because they (1) are part of the same plate boundary with similar kinematics, (2) are under similar overall stress state, and (3) represent both mature (i.e. SA) and incipient (i.e. WL) plate-boundary faults systems (Atwater, 1970; DeMets, Gordon, Stein, & Argus, 1987; Faulds, Henry, & Hinz, 2005; Wesnousky, 2005).

2 | STRESS-SHADOW MODEL

We use a stress-shadow model to describe the formation of parallel strike-slip faults (Lachenbruch, 1961; Pollard & Segall, 1987) (Figure 2). This model assumes that the crust is under some remote shear stress σ_s^r that exceeds the shear-fracture strength of the deforming crust *Y*, causing strike-slip fault formation. The presence of the fault imposes a local low-stress boundary condition, as the shear stress σ_s decreases to the fault-plane shear stress σ^f (Figure 2). Moving away from the fault, σ_s rises toward σ_s^r, and the distance from the fault when $\sigma_s \geq Y$ is the stress-shadow length *S*. A new strike-slip fault is expected to form only at a distance >*S* from a previously formed fault (Figure 2).

Detailed stress-shadow derivations are provided in Zuza et al. (2017). In this model, the deforming crust behaves as a perfectly plastic medium at the depth- and time-scales of interest. Rock deformation may behave elastically in lower-stress conditions but once stress exceeds the elastic limit of the crust, non-recoverable plastic deformation occurs (Figure 3). With a high enough stress magnitude, brittle failure occurs following the Coulomb-fracture criterion (Figure 3). We ignore the low-strain elastic deformation and model the deforming crust as completely plastic, controlled by the Coulomb-

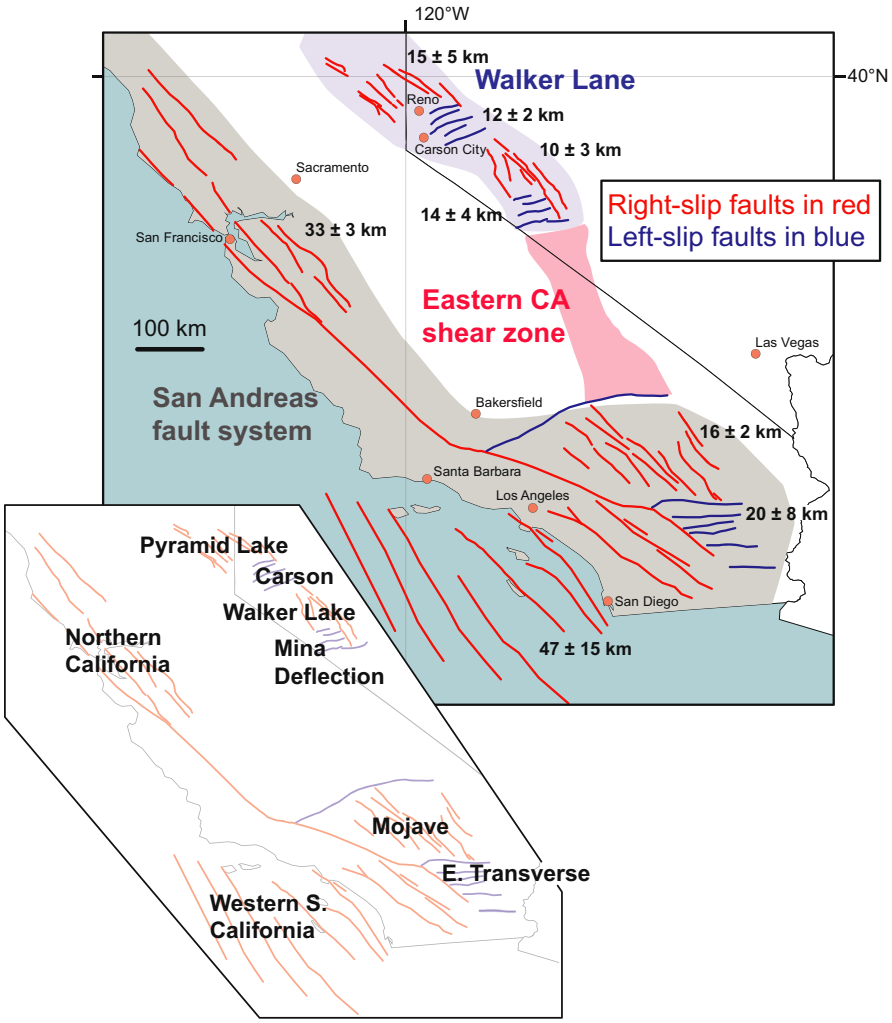

FIGURE 1 Parallel strike-slip fault domains (Faulds & Henry, 2008; Stewart, 1988) in the San Andreas and Walker Lane fault systems (Faulds & Henry, 2008; Wesnousky et al., 2012). Numbers correspond to average spacing (Zuza et al., 2017; this study). Inset shows the names of each strike-slip fault domain

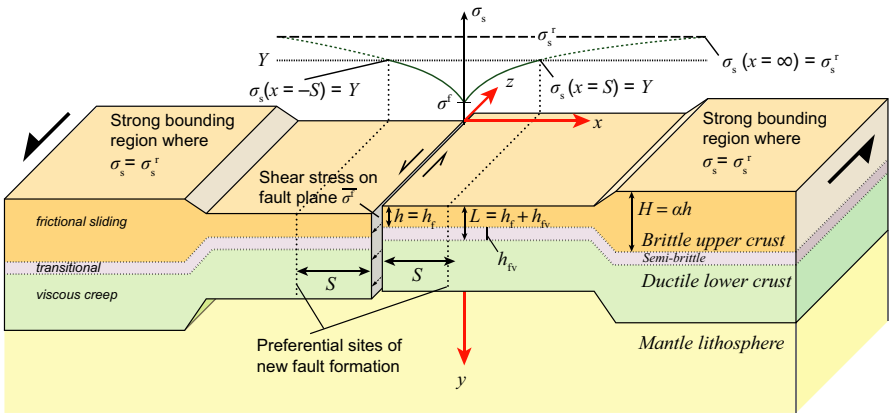

FIGURE 2 Model for parallel strike-slip fault formation via the stress-shadow mechanism, modified from Zuza et al. (2017). The boundary conditions $\sigma_s(x = 0) = \sigma^f$ and $\sigma_s\ (x = \infty) = \sigma_s^r$ are satisfied by off-fault shear stress σ_s. Parameters: σ^f: shear stress on the fault; $\overline{\sigma^f}$: vertically averaged shear strength of the fault; σ_s^r: regional shear stress in the brittle crust; S: stress-shadow length equal to fault spacing; Y: shear-fracture strength of the deforming strike-slip fault domain; h: brittle-crust thickness in the region of strike-slip faulting; H: brittle-crust thickness of the stronger bounding region; L: seismogenic zone thickness, including regimes of frictional sliding (h_f) and transitional frictional sliding and viscous creep (h_{fv}); $\alpha = H/h$

fracture criterion (Figure 3). We also assume that crustal strength resides dominantly in the brittle crust (Jackson, McKenzie, Priestley, & Emmerson, 2008; Lister & Davis, 1989). Thus, crustal stress and strength are approximately linearly depth dependent (Figure 3). Brittle-crust thickness may be constrained by empirical and theoretical yield envelopes (Goetze & Evans, 1979), but parameter variability

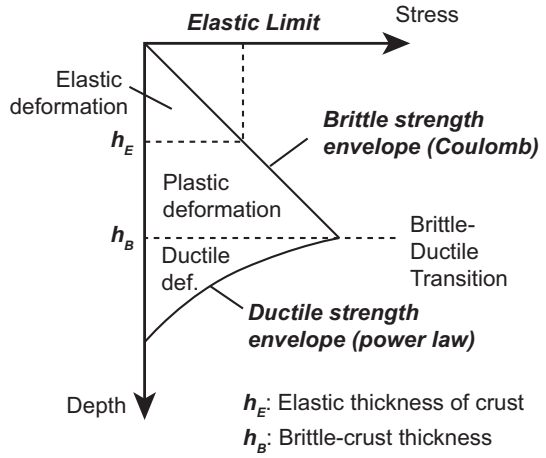

FIGURE 3 Idealized depth-dependent rheological profile for deforming crust, including elastic- and brittle-crust thicknesses

(e.g. grain size or strain rate) and a potentially diffuse brittle–ductile transition zone (Carter & Tsenn, 1987; Pec, Stünitz, Heilbronner, & Drury, 2016) make these estimates imprecise. Here, we use the seismogenic zone to approximate the brittle-crust thickness (Chiarabba & De Gori, 2016; Nazareth & Hauksson, 2004; Williams, 1996).

Previous analyses of fault spacing S and brittle-layer thickness h in California, central Asia, and scaled analogue experiments showed that S and h are linearly related (Zuza et al., 2017). The simplified, linear stress-shadow solution for parallel strike-slip fault formation is:

$$S = \frac{\bar{Y} - \overline{\sigma^f}}{\sigma_s^r - \bar{Y}} h \tag{1}$$

where $\bar{Y}$ and $\overline{\sigma^f}$ are the vertically averaged shear-fracture strength of the deforming brittle crust and shear stress on the fault surface, respectively. Because shear stress/strength vary linearly with brittle-crust thickness (Figure 3), we use the thickness of the thicker (i.e. stronger) crust bounding the faulting domains to quantitatively approximate σ_s^r. Specifically, if the region where strike-slip faults are forming is bounded by stronger crust that is not developing strike-slip faults, then σ_s^r is at or below $\bar{Y}$ of this thicker bounding crust with thickness H (Figure 2). The ratio of H to h, defined by $\alpha = H/h$, can be used to estimate an upper limit of σ_s^r relative to $\bar{Y}$.

Vertical integration of the parameters σ_s^r, $\bar{Y}$, and $\overline{\sigma^f}$—assuming pressure-/depth-dependence—involves cohesive-strength terms for the fault-bounded crust (C_0), faults (C_1) and bounding regions (C_2):

$$\bar{Y} = C_0 + \frac{1}{2}\overline{\mu_\varphi}\rho g h \tag{2}$$

$$\overline{\sigma_f} = C_1 + \frac{1}{2}\overline{\mu_f}\rho g h \tag{3}$$

and

$$\sigma_s^r = C_2 + \frac{1}{2}\overline{\mu_\varphi}\alpha\rho g h \tag{4}$$

where $\overline{\mu_\varphi}$ and $\overline{\mu_f}$ are the effective coefficients of internal and fault friction, respectively. Our interests are in the S/h ratio of continental strike-slip faults—a value which is unaffected by the relative differences in cohesive-strength values (Zuza et al., 2017)—and, accordingly, we ignore these terms in the following fault-spacing relationship:

$$S = \frac{\overline{\mu_\varphi} - \overline{\mu_f}}{\overline{\mu_\varphi}(\alpha - 1)} h \tag{5}$$

3 | METHODS AND DATA

Our analysis requires knowledge of the spacing of major strike-slip faults and the seismogenic thickness L of each faulting domain (i.e. our proxy for h). We are only interested in the spacing of strike-slip faults that individually cut through the entire brittle crust (i.e. not fault splays rooting to a common vertical shear zone at depth). For example, we note that in the WL there are numerous regions with minor strike-slip faults with spacings of ~1 km (e.g. western Mina Deflection; Nagorsen-Rinke, Lee, & Calvert, 2013), but it is unlikely that these fault splays remain independent to >10 km depth. Without subsurface information for each fault, we use an arbitrary cutoff criterion to objectively avoid minor structures. We only considered faults with a length >75% of the fault-perpendicular width of the fault domain. Average fault spacing along the SA was tabulated in Zuza et al. (2017) following the same methods used here. For WL, we examined published maps (Dong et al., 2014; Faulds & Henry, 2008; Gold et al., 2013; Nagorsen-Rinke et al., 2013; Stewart, 1999) (Figure 1). A detailed discussion of WL faults can be found in the Supporting Information. The fault-perpendicular distance between faults was measured; average spacing and standard deviation are given in Table 1.

TABLE 1 Observed fault spacing and seismogenic zone thickness in western North America

	D95 thickness (km)	±σ	Fault spacing (km)	±σ	Ref.
San Andreas fault system					
Northern California	14.4	1.9	33	3	1
Western Southern California	15.7	1.1	47	15	2
Mojave	11.9	1.1	16	2	3
Eastern Transverse Range	12.1	1.5	20	8	2
Best-fit linear regression of seismogenic thickness vs. fault spacing for California					
S = 7.7 (±4.5)L – 74.7 (±57.6)					
Walker Lane fault system					
Pyramid Lake Domain	14.3	1.4	15	5	4,5
Carson Domain	10.5	0.6	12	2	5,6
Walker Lake Domain	9.6	1.9	10	3	5
Mina Deflection	11.2	0.7	14	4	7
Best-fit linear regression of seismogenic thickness vs. fault spacing for Walker Lane					
S = 1.1 (±1.4)L – 0.4 (±14.8)					

Sources: 1. Savage and Lisowski (1993); 2. Dickinson (1996); 3. Dokka and Travis (1990); 4. Gold et al. (2013); 5. Faulds and Henry (2008); 6. Stewart (1999); 7. Nagorsen-Rinke et al. (2013).

Note that previous publications regarding the Carson Domain (Figure 1) report three E–NE-striking left-slip faults (i.e. the Olinghouse fault, Carson lineament, and Wabuska lineament) (Faulds & Henry, 2008). However, our observations of published maps (Stewart, 1999) and the geology suggest that there may be two additional, potentially inactive, E–NE-striking faults (see Supporting Information for evidence). In the fault-spacing analysis, we discuss the implications of these additional strike-slip faults.

The seismogenic zone thickness L was determined using relocated earthquake data, with vertical uncertainties of <1 km (Hauksson, Yang, & Shearer, 2012; Lin, Shearer, & Hauksson, 2007; Schaff & Waldhauser, 2005; Waldhauser & Schaff, 2008) (Figure 4). Earthquake events were projected onto a fault-perpendicular vertical plane (Figure 4). The cutoff depths above which 95% (D95) of the observed seismicity occurs were calculated for set-length segments (l = 25 km), and the resulting values were averaged for each profile (Figure 4).

4 | RESULTS

Figure 5 plots average fault spacing S against the seismogenic zone thickness L for the San Andreas and Walker Lane fault systems. Note that we present two data points for the Carson Domain: one that includes S observations based on the three traditionally defined Carson faults and one based on our reinterpretation of two additional faults (Figure 5). If we ignore the Carson data entirely, the remaining three fault domains (i.e. Pyramid Lake, Walker Lake, and the Mina Deflection) show a clear linear relationship (thick green dashed line in Figure 5). The original three-fault Carson data point plots significantly off this line, whereas the reinterpreted five-fault data point plots in line with the other data (Figure 5). Based on these observations and our preliminary geologic investigations, we suggest that a five-fault Carson Domain better represents this system within the Walker Lane. The following discussion assumes the reinterpreted data point for the Carson Domain.

Both the San Andreas and Walker Lane fault systems show linear S/L relationships (Figure 5). The S/L slope is steeper for the SA data than for the WL system: ~8 vs. 1, respectively. The axis intercepts for the two linear regressions differ significantly. The SA curve has a negative vertical-axis intercept of $S = 75 \pm 58$ km, whereas the WL curve has an S-axis intercept of 0 ± 15 km (Figure 5). The ~9.7 km horizontal-axis (L-axis) intercept for the SA curve predicts that for a single fault strand in the SA system—such as the central San Andreas fault—the seismogenic zone thickness at the fault should be 9–10 km, which is supported by relocated seismicity (Lin et al., 2007).

5 | DISCUSSION AND SUMMARY

To relate strike-slip fault observations to the stress-shadow model (Equation 5), we assume $L = h$. However, L could overestimate h if L actually consists of a frictional-sliding layer (h_f) and a transitional zone (h_{fv}) of frictional sliding and viscous creeping ($L = h_f + h_{fv}$) (Figure 2). A diffuse brittle–ductile transition zone would, for a given fault system, shift the S/L curve right compared with an S/h plot because $L \geq h$. The linear slope should not change. That said, the WL S/L curve has a zero S-intercept (Figure 5). This suggests it was not shifted by L overestimating h, or else the inferred S/h curve would have a positive S-axis intercept, which is not observed in other continental settings or analogue experiments (Zuza et al., 2017).

Given $h \approx L$, the S/h slope can constrain regional stress magnitude (α) and the effective coefficient of fault friction ($\overline{\mu_f}$) following our stress-shadow model. However, we note that absolute solutions for α and $\overline{\mu_f}$ are highly sensitive to the chosen parameters, and therefore we are most interested in relative differences between these values. Rearranging Equation (5) and using the observed S/h slope for each fault system, we plot $\alpha(\overline{\mu_f})$ (Figure 6a). In the Sierran and Western Transverse blocks (i.e. areas without active parallel strike-slip faults) H = 16–17 km (Zuza et al., 2017); thus α is ~1.6–1.2 and ~1.3–1.1 for WL and SA, respectively. We expect that the lowest α for each fault system represents the effective remote stress driving stress-shadow faulting. The estimated bulk friction coefficient for the SA faults is lower ($\overline{\mu_f}$ = 0.06) than for WL faults ($\overline{\mu_f}$ = 0.19) (Figure 6a). Alternatively, if α = 1.1 for both systems, $\overline{\mu_f}$ is 0.06 and 0.22 for SA and WL, respectively.

To examine possible ranges of α and $\overline{\mu_f}$, and demonstrate how parameter variations affect the S/h slope, we plot S–h data against modeled stress-shadow solutions using the above constraints as parameter bounds (Figure 6b,c). First, we assume that an equal regional shear stress is acting on both systems. The α proxy is an upper bound, as originally defined, and we choose the lowest α value common to both fault systems, α = ~1.15 (Figure 6b). This plot shows that the SA faults ($\overline{\mu_f}$ = 0.19–0.13) are relatively weaker than those in the WL system ($\overline{\mu_f}$ = 0.20). Alternatively, if we fix fault friction as a constant across all faults (i.e. $\overline{\mu_f}$ = 0.18), we can explore the relative difference in the α required to produce the observed S–h relationship (Figure 6c). The α values overlap, although the SA α is slightly lower than the WL α: 1.1 ± 0.1 vs. ~1.2 respectively. Note

FIGURE 4 (a) Earthquake-location data for California used in this study from Schaff and Waldhauser (2005), Lin et al. (2007), Waldhauser and Schaff (2008), and Hauksson et al. (2012). Lines and letters represent the locations of earthquake-depth profiles plotted in (b–e). (b–e) Earthquake depth plotted as a function of horizontal distance across the Walker Lane fault domains. Profiles are oriented orthogonal to the strike-slip faults in each domain. In each plot, the cutoff depth above which 95% (D95) of seismicity is contained in the crust was calculated. Dashed blue line represents the bulk average D95 depth, whereas the solid red lines represent the D95 depths in each segment of length l (dashed red line indicates larger l to accommodate remaining earthquake events that do not warrant an additional segment analysis)

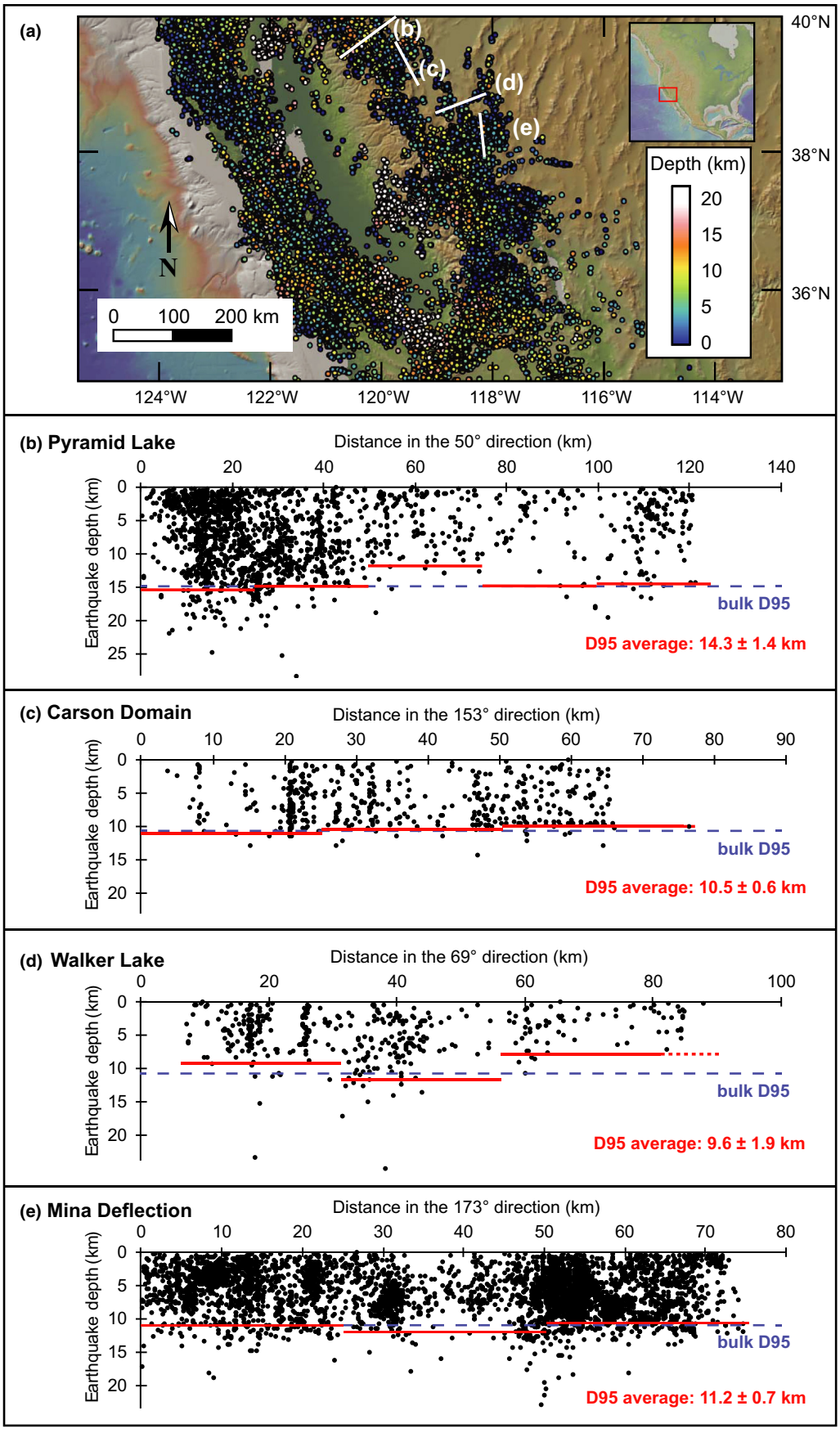
(a)
(b)
(c)
(d)
(e)
Depth (km)
20
15
10
5
0
N
0 100 200 km
40°N
38°N
36°N
124°W
122°W
120°W
118°W
116°W
114°W
(b) Pyramid Lake
Distance in the 50° direction (km)
Earthquake depth (km)
bulk D95
D95 average: 14.3 ± 1.4 km
(c) Carson Domain
Distance in the 153° direction (km)
bulk D95
D95 average: 10.5 ± 0.6 km
(d) Walker Lake
Distance in the 69° direction (km)
bulk D95
D95 average: 9.6 ± 1.9 km
(e) Mina Deflection
Distance in the 173° direction (km)
bulk D95
D95 average: 11.2 ± 0.7 km

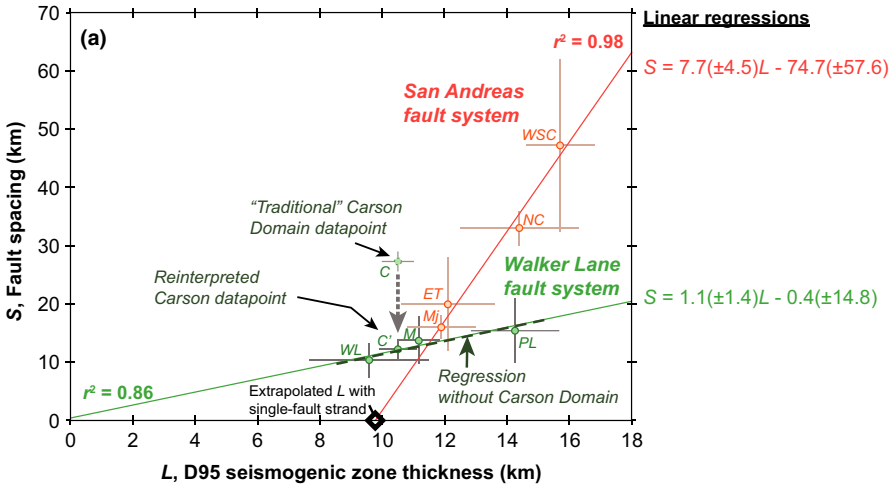

FIGURE 5 (a) Seismogenic zone thickness *L* plotted against fault spacing *S* for the SA and WL. See text for discussion regarding the Carson data point. Lines represent best-fit linear regressions to the data. Italicized letters indicate which domain each data point represents: C and C′, Carson Domain and relocated Carson Domain; ET, Eastern Transverse; M, Mina Deflection; Mj, Mojave; NC, Northern California; PL, Pyramid Lake Domain; WL, Walker Lake Domain; WSC, Western Southern California

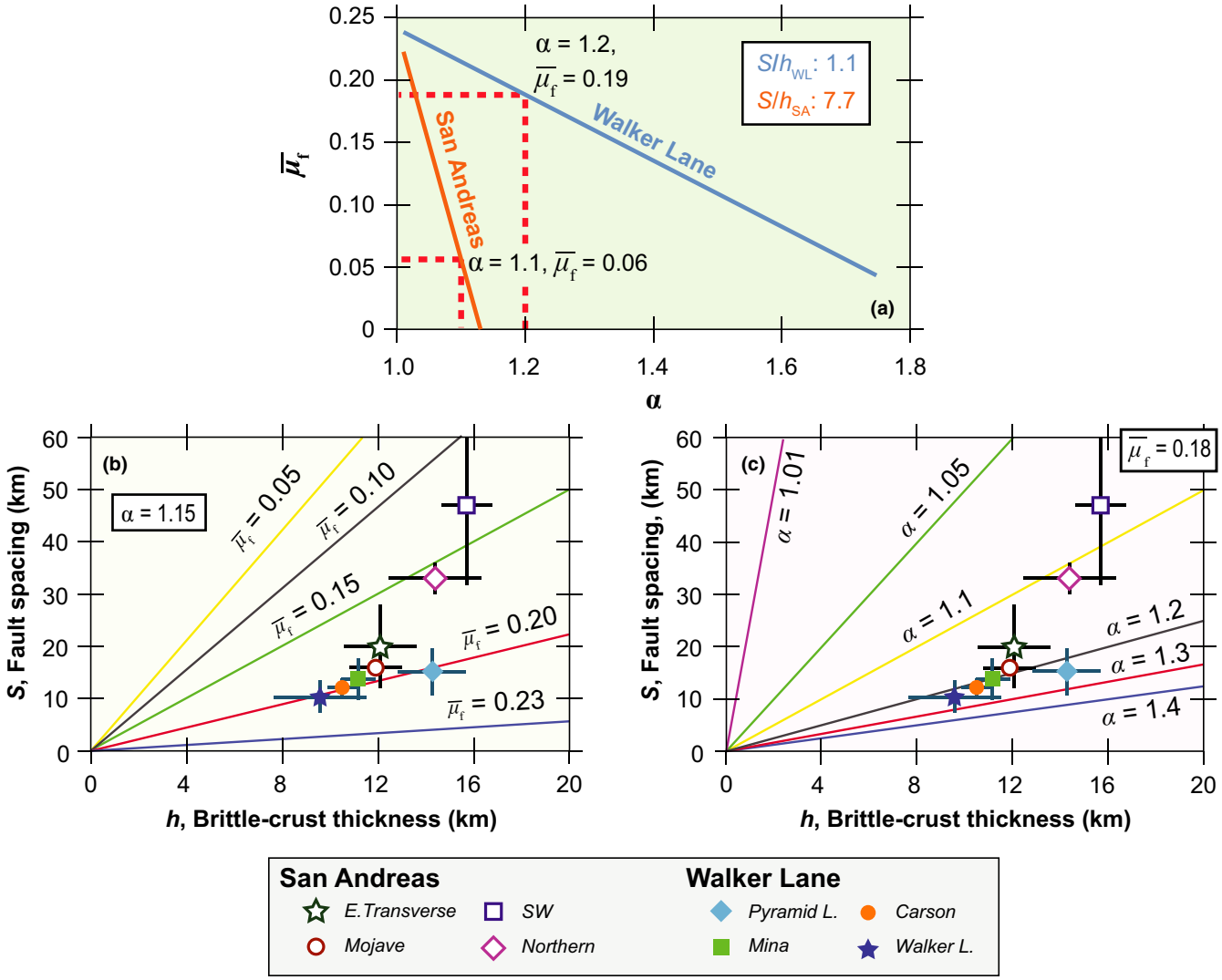

FIGURE 6 (a) Range of values according to our stress-shadow model, showing $\overline{\mu_f}$ as a function of α, based on observed *S*/*h* slope from SA and WL data. Dashed lines encompass range of observed α for each fault system. (b,c) Modeled relationships between *S* and *h* for varying (b) $\overline{\mu_f}$ and (c) α values. $\overline{\mu_\varphi}$ is fixed at 0.24 (Jaeger, Cook, & Zimmerman, 2009)

that the *S*/*h* curve of the WL faults has a near-zero *S*-intercept and its slope parallels parameter contours, implying that the WL fault domains have similar α and $\overline{\mu_f}$ values, whereas the SA *S*/*h* curve crosses parameter contours, suggesting that these values vary between the fault domains (Figure 6b,c). Our overall low fault-friction estimates (0.2–0.1) (Figure 6) are consistent with previous studies (e.g. Bird & Kong, 1994; Fay & Humphreys, 2006).

The significant dissimilarities between the SA and WL *S*/*L* curves (i.e. their intercepts and slopes) are probably related to different mechanical properties of the strike-slip faults and the fault-hosting crust. We envision several possibilities for how the local geology or regional boundary conditions may affect the *S*–*L* relationships of a given strike-slip fault system, including its slope and/or *S*- and *L*-axes intercepts.

The steeper SA curve relative to WL may reflect lower fault friction because the fault-hosting crust in western California contains friction-reducing clays and hydrated phyllosilicates (Collettini, Niemeijer, Viti, & Marone, 2009) of forearc/mélange materials (Dickinson, 1981) (Figure 7a). A lower effective shear stress may act on the SA faults (Figure 7a). A lower strain rate ($\dot{\varepsilon}$) in WL predicts lower $\bar{Y}$ (Goetze & Evans, 1979) and therefore lower *S*/*h* slope (see Equation 1). The negative *y*-intercept of the SA faults suggests that the *S*/*L* curve, relative to WL, is translated right or down with a thicker seismogenic zone *L* or smaller spacing *S*, respectively (Figure 7b). Apparent spacing decreases may be due to fault-healing effects (Tenthorey & Cox, 2006) or abandonment of faults and activation of new ones as fault-bounded blocks rotate (Carlson, Pluhar, Glen, & Farner, 2013), making certain previously active faults unfavorable.

With higher strain, *L* in SA may be larger because the base of the brittle crust developed asperities protruding into the underlying viscous medium (Figure 7b); earthquakes would still occur in this mixed frictional–viscous zone, increasing *L* (Pec et al., 2016). A thicker *L* is also predicted by higher $\dot{\varepsilon}$ across the SA (Goetze & Evans, 1979) (Figure 7b). Alternatively, the *S*/*L* curve difference may be a result of higher heat flow for the WL in the Basin and Range province (Blackwell et al., 2011; Bonner, Blackwell, & Herrin, 2003), which would result in a thinner *L*. This would effectively shift the *S*/*L* curve left without affecting its slope (Figure 7c).

The WL and SA strike-slip faults are earthquake hazards. Minimal vertical offset and relatively slow slip rates on these faults have made assessment of their slip histories and seismic risk problematic (Wesnousky, Bormann, Kreemer, Hammond, & Brune, 2012). The methods presented here of using *S* and *L* observations to evaluate fault friction may help evaluate relative risk among strike-slip faults (e.g. slip may be focused on faults with lower fault friction, or greater elastic loading may occur on faults with higher friction). Furthermore, estimates of fault characteristics can improve physics-based models of the earthquake cycle and hazards (e.g. Console, Carluccio, Papadimitriou, & Karakostas, 2015; Pagani et al., 2014; Petersen et al., 2015).

Our strike-slip fault spacing investigation of the Walker Lane and San Andreas systems reveals that both display linear *S*/*L* relationships, but the SA curve has a steeper slope and negative *S*-axis intercept. Assuming a stress-shadow mechanism, we explored what these *S*/*L* curve differences mean for fault strength and regional shear stresses. This analysis suggests that fault friction of San

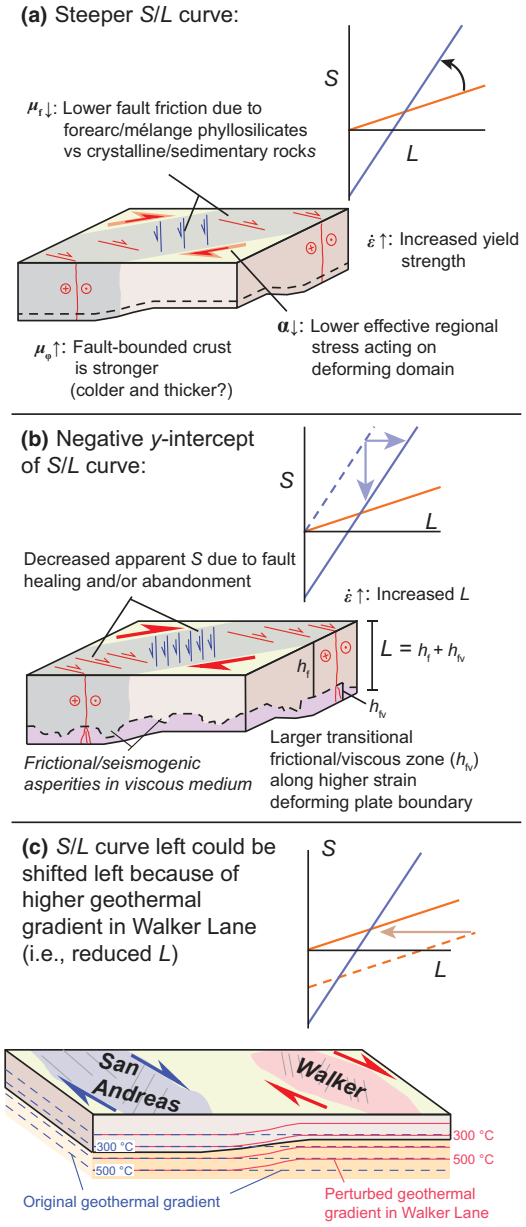

FIGURE 7 Models to explain the mechanical differences between the San Andreas and Walker Lane fault systems, including their different *S*/*L* curves (San Andreas: blue lines; Walker Lane: orange lines). (a) The steeper *S*/*L* SA curve may reflect the local geology of the fault-bounding crust or different boundary conditions. (b) The negative *S*-axis intercept of the SA curve could suggest a shift in *L* or *S* relative to the WL fault system. (c) The elevated heat flow in WL may have decreased *L*, shifting the *S*/*L* curve toward a zero *S*-intercept. Note that models are not to scale; see text for discussion

Andreas strike-slip faults may be lower than that of Walker Lane faults. Variations in the local geology of the fault-hosting crust and/or the regional boundary conditions may affect the observed mechanical differences between the SA and WL fault systems, but future research is needed to test our model constraints.

ACKNOWLEDGEMENTS

Startup funds at UNR supported this research. Comments from Alain Tremblay, an anonymous reviewer, and Scientific Editor Jean Braun greatly improved the presentation of our ideas in this manuscript.

REFERENCES

Atwater, T. (1970). Implications of plate tectonics for the Cenozoic tectonic evolution of western North America. *Geological Society of America Bulletin*, *81*, 3513–3536. https://doi.org/10.1130/0016-7606(1970)81[3513:IOPTFT]2.0.CO;2

Bird, P., & Kong, X. (1994). Computer simulations of California tectonics confirm very low strength of major faults. *Geological Society of America Bulletin*, *106*, 159–174. https://doi.org/10.1130/0016-7606(1994)106<0159:CSOCTC>2.3.CO;2

Blackwell, D., Richards, M., Frone, Z., Batir, J., Ruzo, A., Dingwall, R., & Williams, M. (2011). Temperature at depth maps for the conterminous US and geothermal resource estimates. *GRC Transactions*, *35*, 1545–1550.

Bonner, J. L., Blackwell, D. D., & Herrin, E. T. (2003). Thermal constraints on earthquake depths in California. *Bulletin of the Seismological Society of America*, *93*, 2333–2354. https://doi.org/10.1785/0120030041

Carlson, C. W., Pluhar, C. J., Glen, J. M., & Farner, M. J. (2013). Kinematics of the west-central Walker Lane: Spatially and temporally variable rotations evident in the Late Miocene Stanislaus Group. *Geosphere*, *9*, 1530–1551. https://doi.org/10.1130/GES00955.1

Carter, N. L., & Tsenn, M. C. (1987). Flow properties of continental lithosphere. *Tectonophysics*, *136*, 27–63. https://doi.org/10.1016/0040-1951(87)90333-7

Chiarabba, C., & De Gori, P. (2016). The seismogenic thickness in Italy: Constraints on potential magnitude and seismic hazard. *Terra Nova*, *28*, 402–408. https://doi.org/10.1111/ter.12233

Collettini, C., Niemeijer, A., Viti, C., & Marone, C. (2009). Fault zone fabric and fault 206 weakness. *Nature*, *462*, 907–910. https://doi.org/10.1038/nature08585

Console, R., Carluccio, R., Papadimitriou, E., & Karakostas, V. (2015). Synthetic earthquake catalogs simulating seismic activity in the Corinth Gulf, Greece, fault system. *Journal of Geophysical Research: Solid Earth*, *120*, 326–343.

Davy, P., & Cobbold, P. R. (1988). Indentation tectonics in nature and experiment. 1. Experiments scaled for gravity. *Bulletin of the Geological Institution of the University of Uppsala*, *14*, 129–141.

DeMets, C., Gordon, R., Stein, S., & Argus, D. (1987). A revised estimate of Pacific-North America motion and implications for western North America plate boundary zone tectonics. *Geophysical Research Letters*, *14*, 911–914. https://doi.org/10.1029/GL014i009p00911

Dickinson, W. R. (1981). Plate tectonic evolution of the southern Cordillera. Relations of tectonics to ore deposits in the southern Cordillera. *Arizona Geological Society Digest*, *14*, 113–135.

Dickinson, W. R. (1996). Kinematics of transrotational tectonism in the California Transverse Ranges and its contribution to cumulative slip along the San Andreas transform fault system. *Geological Society of America Special Paper*, *305*, 1–46.

Dokka, R. K., & Travis, C. J. (1990). Late Cenozoic strike-slip faulting in the Mojave Desert, California. *Tectonics*, *9*, 311–340. https://doi.org/10.1029/TC009i002p00311

Dong, S., Ucarkus, G., Wesnousky, S. G., Maloney, J., Kent, G., Driscoll, N., & Baskin, R. (2014). Strike-slip faulting along the Wassuk Range of the northern Walker Lane, Nevada. *Geosphere*, *10*, 40–48. https://doi.org/10.1130/GES00912.1

Faulds, J. E., & Henry, C. D. (2008). Tectonic influences on the spatial and temporal evolution of the Walker Lane: An incipient transform fault along the evolving Pacific-North American plate boundary. *Arizona Geological Society Digest*, *22*, 437–470.

Faulds, J. E., Henry, C. D., & Hinz, N. H. (2005). Kinematics of the northern Walker Lane: An incipient transform fault along the Pacific–North American plate boundary. *Geology*, *33*, 505–508. https://doi.org/10.1130/G21274.1

Fay, N., & Humphreys, E. (2006). Dynamics of the Salton block: Absolute fault strength and crust–mantle coupling in Southern California. *Geology*, *34*, 261–264. https://doi.org/10.1130/G22172.1

Goetze, C., & Evans, B. (1979). Stress and temperature in the bending lithosphere as constrained by experimental rock mechanics. *Geophysical Journal International*, *59*, 463–478. https://doi.org/10.1111/j.1365-246X.1979.tb02567.x

Gold, R. D., Stephenson, W. J., Odum, J. K., Briggs, R. W., Crone, A. J., & Angster, S. J. (2013). Concealed Quaternary strike-slip fault resolved with airborne lidar and seismic reflection: The Grizzly Valley fault system, northern Walker Lane, California. *Journal of Geophysical Research: Solid Earth*, *118*, 3753–3766.

Hauksson, E., Yang, W., & Shearer, P. M. (2012). Waveform relocated earthquake catalog for southern California (1981 to June 2011). *Bulletin of the Seismological Society of America*, *102*, 2239–2244. https://doi.org/10.1785/0120120010

Jackson, J., McKenzie, D., Priestley, K., & Emmerson, B. (2008). New views on the structure and rheology of the lithosphere. *Journal of the Geological Society*, *165*, 453–465. https://doi.org/10.1144/0016-76492007-109

Jaeger, J. C., Cook, N. G., & Zimmerman, R., 2009. *Fundamentals of Rock Mechanics*. 475 p.

Lachenbruch, A. H. (1961). Depth and spacing of tension cracks. *Journal of Geophysical Research*, *66*, 4273–4292. https://doi.org/10.1029/JZ066i012p04273

Lin, G., Shearer, P. M., & Hauksson, E. (2007). Applying a three-dimensional velocity model, waveform cross correlation, and cluster analysis to locate southern California seismicity from 1981 to 2005. *Journal of Geophysical Research: Solid Earth*, *112* (B12), 425.

Lister, G. S., & Davis, G. A. (1989). The origin of metamorphic core complexes and detachment faults formed during Tertiary continental extension in the northern Colorado River region, USA. *Journal of Structural Geology*, *11*, 65–94. https://doi.org/10.1016/0191-8141(89)90036-9

Martel, S. J., & Pollard, D. D. (1989). Mechanics of slip and fracture along small faults and simple strike-slip fault zones in granitic rock. *Journal of Geophysical Research*, *94*, 9417–9428. https://doi.org/10.1029/JB094iB07p09417

Nagorsen-Rinke, S., Lee, J., & Calvert, A. (2013). Pliocene sinistral slip across the Adobe Hills, eastern California–western Nevada: Kinematics of fault slip transfer across the Mina deflection. *Geosphere*, *9*, 37–53.

Nazareth, J. J., & Hauksson, E. (2004). The seismogenic thickness of the southern California crust. *Bulletin of the Seismological Society of America*, *94*, 940–960. https://doi.org/10.1785/0120020129

Pagani, M., Monelli, D., Weatherill, G., Danciu, L., Crowley, H., Silva, V., … Vigano, D. (2014). OpenQuake engine: An open hazard (and risk) software for the global earthquake model. *Seismological Research Letters*, *85*, 692–702. https://doi.org/10.1785/0220130087

Pec, M., Stünitz, H., Heilbronner, R., & Drury, M. (2016). Semi-brittle flow of granitoid fault rocks in experiments. *Journal of Geophysical Research: Solid Earth*, *121* (3), 1677–1705.

Petersen, M. D., Moschetti, M. P., Powers, P. M., Mueller, C. S., Haller, K. M., Frankel, A. D., … Olsen, A. H. (2015). The 2014 United States national seismic hazard model. *Earthquake Spectra*, *31*, S1–S30. https://doi.org/10.1193/120814EQS210M

Pollard, D. D., & Segall, P. (1987). Theoretical displacements and stresses near fractures in rock: With applications to faults, joints, veins, dikes, and solution surfaces. *Fracture Mechanics of Rocks*, 277–349. https://doi.org/10.1016/B978-0-12-066266-1.50013-2

Savage, J. C., & Lisowski, M. (1993). Inferred depth of creep on the Hayward fault, central California. *Journal of Geophysical Research: Solid Earth*, *98*, 787–793. https://doi.org/10.1029/92JB01871

Schaff, D. P., & Waldhauser, F. (2005). Waveform cross-correlation-based differential travel-time measurements at the Northern California Seismic Network. *Bulletin of the Seismological Society of America*, *95*, 2446–2461. https://doi.org/10.1785/0120040221

Segall, P., & Pollard, D. D. (1983). Nucleation and growth of strike slip faults in granite. *Journal of Geophysical Research: Solid Earth*, *88*, 555–568. https://doi.org/10.1029/JB088iB01p00555

Stewart, J. H. (1988). Tectonics of the Walker Lane belt, western Great Basin: Mesozoic and Cenozoic deformation in a zone of shear. In W. G. Ernst (Ed.), Rubey Volume. *Metamorphism and crustal evolution of the western United States* (pp. 681–713). Old Tappan, N.J.: Prentice-Hall.

Stewart, J. H. (1999). *Geologic Map of the Carson City 30 X 60 Minute Quadrangle, Nevada*. Reno, NV: Nevada Bureau of Mines and Geology.

Tenthorey, E., & Cox, S. F. (2006). Cohesive strengthening of fault zones during the inter-seismic period: An experimental study. *Journal of Geophysical Research*, *111* (B9), 3051. https://doi.org/10.1016/j.epsl.2016.09.041

Waldhauser, F., & Schaff, D. P. (2008). Large-scale relocation of two decades of Northern California seismicity using cross-correlation and double-difference methods. *Journal of Geophysical Research: Solid Earth*, *113* (B8), 501.

Wesnousky, S. G. (2005). The San Andreas and Walker Lane fault systems, western North America: Transpression, transtension, cumulative slip and the structural evolution of a major transform plate boundary. *Journal of Structural Geology*, *27*, 1505–1512. https://doi.org/10.1016/j.jsg.2005.01.015

Wesnousky, S. G., Bormann, J. M., Kreemer, C., Hammond, W. C., & Brune, J. N. (2012). Neotectonics, geodesy, and seismic hazard in the Northern Walker Lane of Western North America: Thirty kilometers of crustal shear and no strike-slip? *Earth and Planetary Science Letters*, *329*, 133–140. https://doi.org/10.1016/j.epsl.2012.02.018

Williams, C. F. (1996). Temperature and the seismic/aseismic transition: Observations from the 1992 Landers earthquake. *Geophysical Research Letters*, *23*, 2029–2032. https://doi.org/10.1029/96GL02066

Yin, A., Zuza, A. V., & Pappalardo, R. T. (2016). Mechanics of evenly spaced strike-slip faults and its implications for the formation of tiger-stripe fractures on Saturn's moon Enceladus. *Icarus*, *266*, 204–216. https://doi.org/10.1016/j.icarus.2015.10.027

Zuza, A. V., Yin, A., Lin, J., & Sun, M. (2017). Spacing and strength of active continental strike-slip faults. *Earth and Planetary Science Letters*, *457*, 49–62.

SUPPORTING INFORMATION

Additional Supporting Information may be found online in the supporting information tab for this article.

Data S1 Discussion of fault domains in the Walker Lane.

Figure S1 Evenly spaced parallel strike-slip fault domains in the Walker Lane. Fault data from Stewart (1999), Wesnousky (2005), Faulds and Henry (2008), Wesnousky et al. (2012), and Gold et al. (2013). Note that normal faults and smaller structures are omitted for clarity.

Figure S2 (a) Topography of the Carson Domain in the Walker Lane. The three previously recognized northeast-trending structures are shown (i.e. the Olinghouse fault, Carson lineament, and Wabuska lineament) in addition to two previously undocumented parallel lineaments. Also shown are the locations of Supporting Figures 2b–e. (b) Crop of the geologic map of the Carson City 30′ × 60′ quadrangle (Stewart, 1999), which includes the southwestern part of the Carson Domain. Dashed lines highlight lineaments and faults discussed in the text. Note that the offsets and normal faults along the middle inferred fault are consistent with left-slip kinematics. For individual unit descriptions, please see the original Stewart (1999) reference. Also shown are locations of Supporting Figure 2c and the Google Earth image in Supporting Figure 2f. (c) Unmodified zoom in on portion of Supporting Figure 2b (map of Stewart, 1999) showing two left-lateral offsets of Tads unit (i.e. interbedded Tertiary andesite and sedimentary rocks) consistent with inference that Inferred Fault #2 is a left-lateral strike-slip fault. Also shown are the locations of Supporting Figures 2d,e. (d–f) Remote sensing analyses of the Inferred Fault #2 showing consistent ~300 m left-lateral offset along its strike. Note that unit assignments are from Stewart (1999). (d) ~310 m left-lateral offset of Tads-Tad contact. (e) ~305 m left-lateral offset of Tba-Tads contact. (f) Topographic analysis of normal fault-termination structure showing ~320 m horizontal motion, which is kinematically compatible with similar magnitude left-lateral slip.

How to cite this article: Zuza AV, Carlson CW. What can strike-slip fault spacing tell us about the plate boundary of western North America?. *Terra Nova*. 2017;00:1–9. https://doi.org/10.1111/ter.12315